Stability analysis of an industrial blade accounting for a blade-tip/casing nonlinear interface

Yann Colaïtis, Alain Batailly

▶ **To cite this version:**

Yann Colaïtis, Alain Batailly. Stability analysis of an industrial blade accounting for a blade-tip/casing nonlinear interface. Journal of Engineering for Gas Turbines and Power, In press, 10.1115/1.4055492 . hal-03778471

HAL Id: hal-03778471
https://hal.science/hal-03778471

Submitted on 15 Sep 2022

HAL is a multi-disciplinary open access archive for the deposit and dissemination of scientific research documents, whether they are published or not. The documents may come from teaching and research institutions in France or abroad, or from public or private research centers.

L'archive ouverte pluridisciplinaire **HAL**, est destinée au dépôt et à la diffusion de documents scientifiques de niveau recherche, publiés ou non, émanant des établissements d'enseignement et de recherche français ou étrangers, des laboratoires publics ou privés.

POLYTECHNIQUE MONTRÉAL
UNIVERSITÉ D'INGÉNIERIE

LABORATOIRE D'ANALYSE VIBRATOIRE ET ACOUSTIQUE

Stability analysis of an industrial blade accounting for a blade-tip/casing nonlinear interface

Y. Colaïtis[1], A. Batailly[1]

Abstract

This paper investigates the local stability analysis of periodic solutions corresponding to the nonlinear vibration response of an industrial compressor blade, NASA rotor 37, on which are applied different types of nonlinearities. These solutions are obtained using a harmonic balance method-based approach presented in a previous paper. It accounts for unilateral contact and dry friction of the rotating blade against a rigid casing through a regularized penalty law. A Lanczos filtering technique is also employed to mitigate spurious oscillations related to the Gibbs phenomenon thus enhancing the robustness of the solver. In addition, a component mode synthesis technique is used to reduce the dimension of the numerical model. Stability assessment of the computed solutions relies on Floquet theory. It is performed through the computation of the monodromy matrix as well as Hill's method. Both methodologies are applied and thoroughly compared as the severity of the nonlinearity is gradually increased from a cubic spring to 3D contact conditions on a deformed casing. While the presented results underline the applicability of both stability assessment methodologies for all types of nonlinearities, they also put forward the much higher computational effort required when computing the monodromy matrix. Indeed, it is shown that Hill's method yields converged results for significantly lower values of both the number of retained harmonics and the considered number of time steps thus making it a far more efficient method when dealing with industrial models. It is also underlined that the presented results are in excellent agreement with reference solution points obtained with time domain solution methods. Specific implementation tweaks that were found to be of critical importance in order to efficiently assess the stability of computed solutions are also detailed in order to provide a comprehensive view of the challenges inherent to such numerical developments.

Keywords

harmonic balance method; blade-tip/casing contacts; rotor/stator interaction; Floquet theory; Hill's method; stability analysis

1 - Department of Mechanical Engineering, École Polytechnique de Montréal, P.O. Box 6079, Succ. Centre-Ville, Montréal, Québec, Canada H3C 3A7

Analyse de stabilité d'une aube industrielle impliquant une interface non-linéaire de type aube/carter

Y. Colaïtis[1], A. Batailly[1]

Résumé

Cet article porte sur l'analyse de la stabilité locale de solutions périodiques associées à la réponse vibratoire non-linéaire d'une aube de compresseur industriel, le rotor 37 de la NASA, sur lesquelles sont appliquées différents types de non-linéarités. Ces solutions sont obtenues en utilisant une approche basée sur la méthode de l'équilibrage harmonique présentée dans un article précédent. Elle tient compte du contact unilatéral et du frottement sec de l'aube en rotation avec un carter rigide par le biais d'une loi de pénalité régularisée. Une technique de filtrage de Lanczos y est également utilisée afin d'atténuer les oscillations parasites liées au phénomène de Gibbs, ce qui améliore la robustesse du solveur. En outre, une technique de réduction modale est utilisée pour réduire la dimension du modèle numérique considéré. L'évaluation de la stabilité des solutions calculées repose sur la théorie de Floquet. Elle est effectuée par le calcul de la matrice de monodromie ainsi que par la méthode de Hill. Les deux méthodologies sont appliquées et comparées de manière approfondie lorsque la sévérité de la non-linéarité est progressivement augmentée de ressorts cubiques à des conditions de contact 3D sur un carter déformé. Si les résultats présentés soulignent l'applicabilité des deux méthodologies d'évaluation de la stabilité pour tous les types de non-linéarités, ils mettent également en avant l'effort de calcul beaucoup plus important requis lors du calcul de la matrice de monodromie. En effet, il est démontré que la méthode de Hill donne des résultats convergents pour des valeurs significativement plus faibles du nombre d'harmoniques retenus et du nombre de pas de temps considérés, ce qui en fait une méthode beaucoup plus efficace pour les modèles industriels. Il est également souligné que les résultats présentés font preuve d'un excellent accord avec les solutions de référence obtenues à l'aide d'un algorithme d'intégration temporelle. Les ajustements spécifiques de mise en œuvre qui se sont avérés d'une importance critique pour évaluer efficacement la stabilité des solutions calculées sont également détaillés afin de fournir une vue d'ensemble des défis inhérents à de tels développements numériques.

Mots-clés

méthode de l'équilibrage harmonique ; contacts aube/carter ; interaction rotor/stator ; théorie de Floquet ; méthode de Hill ; analyse de stabilité

1 - Département de génie mécanique, École Polytechnique de Montréal, P.O. Box 6079, Succ. Centre-Ville, Montréal, Québec, Canada H3C 3A7

1 Introduction

The nonlinear vibration response of aircraft engine blades has been the focus of a variety of research investigations over the past decades [1, 2]. One of the reason why this is still a very active field of research relates to the fact that, contrary to other complex mechanical systems, aircraft engine blades feature several nonlinear interfaces. Among these interfaces, particular attention has been paid to the blade/disk friction interface [2], the blade/blade contact interface [3] and the blade-tip/casing contact interface [4, 5]. In addition, in certain stages of an engine, blades' significant amplitudes of vibration may also require to account for geometric nonlinearities [6] thus making these components very challenging to analyze in a comprehensive manner.

Because of the very high relative speeds between stator and rotor components and due to very small operating clearances, the blade-tip/casing contact interface induces specific numerical challenges and requires a very accurate contact treatment procedure. As a consequence, nonlinear vibrations resulting from blade-tip/casing contacts have mostly been investigated using time domain solution methods [4, 7]. To the contrary, frequency methods have been shown to be very accurate and efficient to predict a blade's dynamics accounting for blade/disk friction phenomena [2]. Besides of the fact that this compartmentalization is making it impossible to carry out efficient multi-nonlinear analyses, designers are still facing a roadblock since time domain solution methods are ill-suited to get a qualitative understanding of blade's dynamics undergoing blade-tip/casing contacts.

In this context, the recent development of a harmonic balance method-based approach [8, 9]—referred to as RL-HBM (Regularized-Lanczos Harmonic Balance Method) in the remainder—for the analysis of blade-tip/casing contact interactions is promising. While it may allow to efficiently combine distinct nonlinear interfaces within a homogeneous solution framework, the RL-HBM also opens new avenues to provide designers with a much needed qualitative understanding of blade-tip/casing contacts. Results obtained with the RL-HBM for industrial blade models are in agreement with those obtained with time integration [8]. They also advantageously yield an accurate estimate of a blade's actual nonlinear resonance as it impacts the surrounding casing [9].

The assessment of the local stability of solutions computed with the RL-HBM has not been performed yet. More generally, stability analyses of solutions computed by frequency methods on large industrial models remain a significant computational challenge [10, 11] and has been the focal point of recent research works [12, 13]. In this article, the local stability of solutions computed with the RL-HBM is assessed using the Floquet theory. Two methodologies are employed: one relying on the computation of the monodromy matrix [14, 15] and Hill's method [16, 12]. Presented results are numerically verified by confronting both methodologies for different types of nonlinearities. The relevance of the obtained results is also assessed through a direct comparison with results obtained with time domain solution methods where apparent sudden changes in the blade's vibration response were previously reported [9] but never explained.

The first section of the paper recalls the key steps of the RL-HBM. In the second section, the theory of stability analysis is briefly mentioned for the sake of completeness before the industrial blade model be presented in the third section. In the fourth section, four nonlinear configurations, featuring an increasingly complex numerical treatment are presented on the industrial blade model: from cubic springs along the blade-tip to the enforcement of unilateral contact constraints with a deformed rigid casing and the inclusion of centrifugal effects.

2 Regularized-Lanczos harmonic balance

Further details on the numerical aspects introduced throughout this section may be found in references [17, 9]. The normalized equation of motion of a n-dof nonlinear mechanical system reads:

$$\frac{\alpha}{\beta^2}\mathbf{M}\ddot{\boldsymbol{x}}(t) + \frac{\alpha}{\beta}\mathbf{C}\dot{\boldsymbol{x}}(t) + \alpha\mathbf{K}\boldsymbol{x}(t) + \boldsymbol{f}_{\text{nl}}(\boldsymbol{x}(t), \dot{\boldsymbol{x}}(t), \omega) = \boldsymbol{f}_{\text{ext}}(t, \omega) \tag{1}$$

where $\mathbf{M}$, $\mathbf{C}$, $\mathbf{K}$ are the mass, damping and stiffness matrices, $\boldsymbol{x}$ is the displacement vector, $\boldsymbol{f}_{\text{nl}}$ is the nonlinear forces and $\boldsymbol{f}_{\text{ext}}$ corresponds to the periodic excitation forces of angular frequency ω. The overdots refer to derivatives with respect to time t. Scaling factors α and β are used to enhance floating-point accuracy during numerical computations by normalizing the different quantities in both space and time so that $||\alpha\boldsymbol{x}|| \simeq 1$ and $\omega/\beta \simeq 1$. In the case of blade-tip/casing interactions, α is the average operating clearance and β is the middle of the angular frequency range of interest.

2.1 The Harmonic Balance Method

The HBM relies on the assumption that the solutions $\boldsymbol{x}(t)$ of Eq. (1) may be expressed as H-truncated Fourier series:

$$\boldsymbol{x}(t) \simeq \frac{1}{2}\boldsymbol{a}_0 + \sum_{j=1}^{H} \left[\boldsymbol{a}_j \cos\left(j\omega t\right) + \boldsymbol{b}_j \sin\left(j\omega t\right)\right] \tag{2}$$

where vectorial quantities $\boldsymbol{a}_j$ and $\boldsymbol{b}_j$ are the unknown real Fourier coefficients. Each of these coefficients are defined as follows:

$$\begin{cases} \boldsymbol{a}_j = \left[a_j^1,\, a_j^2,\, \ldots,\, a_j^n\right] & \text{for } j \in [\![0..H]\!] \\ \boldsymbol{b}_j = \left[b_j^1,\, b_j^2,\, \ldots,\, b_j^n\right] & \text{for } j \in [\![1..H]\!] \end{cases} \tag{3}$$

The same spectral decomposition is also applied to forces $\boldsymbol{f}_{\text{nl}}$ and $\boldsymbol{f}_{\text{ext}}$. For the sake of clarity, all Fourier coefficients are gathered in $n(2H+1)$-dimensional vectors resulting in the following frequency-domain variables:

$$\begin{aligned} \tilde{\boldsymbol{x}} &= \left[\,\boldsymbol{a}_0,\, \boldsymbol{a}_1,\, \boldsymbol{b}_1,\, \ldots,\, \boldsymbol{a}_H,\, \boldsymbol{b}_H\,\right]^\top \\ \tilde{\boldsymbol{f}}_{\text{nl}} &= \left[\,\boldsymbol{a}_0^{\text{nl}},\, \boldsymbol{a}_1^{\text{nl}},\, \boldsymbol{b}_1^{\text{nl}},\, \ldots,\, \boldsymbol{a}_H^{\text{nl}},\, \boldsymbol{b}_H^{\text{nl}}\,\right]^\top \\ \tilde{\boldsymbol{f}}_{\text{ext}} &= \left[\,\boldsymbol{a}_0^{\text{ext}},\, \boldsymbol{a}_1^{\text{ext}},\, \boldsymbol{b}_1^{\text{ext}},\, \ldots,\, \boldsymbol{a}_H^{\text{ext}},\, \boldsymbol{b}_H^{\text{ext}}\,\right]^\top \end{aligned} \tag{4}$$

After substituting the displacement vector $\boldsymbol{x}(t)$ of Eq. (2), its derivatives $\dot{\boldsymbol{x}}(t)$ and $\ddot{\boldsymbol{x}}(t)$ as well as forces into Eq. (1), a Fourier-Galerkin projection [11] yields a set of $n(2H+1)$ nonlinear algebraic equations in the frequency domain:

$$\mathbf{R}(\tilde{\boldsymbol{x}}, \omega) = \mathbf{Z}(\omega)\tilde{\boldsymbol{x}} + \tilde{\boldsymbol{f}}_{\text{nl}}(\tilde{\boldsymbol{x}}) - \tilde{\boldsymbol{f}}_{\text{ext}}(\omega) = \mathbf{0} \tag{5}$$

where $\mathbf{Z}(\omega)$ is the dynamic stiffness matrix, a block diagonal matrix accounting for the linear dynamics of the response of the system and is defined as follows:

$$\mathbf{Z}(\omega) = \omega^2 \boldsymbol{\nabla}^2 \otimes \frac{\alpha}{\beta^2}\mathbf{M} + \omega\boldsymbol{\nabla} \otimes \frac{\alpha}{\beta}\mathbf{C} + \mathbf{I}_{2H+1} \otimes \alpha\mathbf{K} \tag{6}$$

where $\otimes$ denotes the Kronecker product and $\mathbf{I}_{2H+1}$ is the identity matrix of size $2H+1$. The matrix $\boldsymbol{\nabla}$ is a frequency-domain differential operator, it is defined as:

$$\boldsymbol{\nabla} = \text{diagblock}(0,\, \boldsymbol{\nabla}_1,\, \ldots,\, \boldsymbol{\nabla}_j,\, \ldots,\, \boldsymbol{\nabla}_H) \quad \text{and} \quad \boldsymbol{\nabla}^2 = \boldsymbol{\nabla}\boldsymbol{\nabla} \tag{7}$$

with the elementary first order derivative matrix $\boldsymbol{\nabla}_j$:

$$\boldsymbol{\nabla}_j = j \begin{bmatrix} 0 & 1 \\ -1 & 0 \end{bmatrix} \text{ for } j \in [\![1..H]\!] \tag{8}$$

Solutions of Eq. (5) may be obtained using a Newton-Raphson algorithm. Starting from an adequate initial guess $\tilde{\boldsymbol{x}}^0$, a converged solution is obtained iteratively:

$$\tilde{\boldsymbol{x}}^{k+1} = \tilde{\boldsymbol{x}}^k + \Delta\tilde{\boldsymbol{x}}^k \quad \text{with} \quad \mathbf{R}^k_{,\tilde{\boldsymbol{x}}}\Delta\tilde{\boldsymbol{x}}^k = -\mathbf{R}^k \tag{9}$$

where $\mathbf{R}^k = \mathbf{R}(\tilde{\boldsymbol{x}}^k, \omega)$ is the residual at iteration k and $\mathbf{R}^k_{,\tilde{\boldsymbol{x}}}$ is the Jacobian matrix of the system with respect to $\tilde{\boldsymbol{x}}^k$:

$$\mathbf{R}^k_{,\tilde{\boldsymbol{x}}} = \frac{\partial \mathbf{R}}{\partial \tilde{\boldsymbol{x}}}(\tilde{\boldsymbol{x}}^k, \omega) = \mathbf{Z}(\omega) + \tilde{\boldsymbol{f}}_{\text{nl},\tilde{\boldsymbol{x}}} = \mathbf{Z}(\omega) + \frac{\partial \tilde{\boldsymbol{f}}_{\text{nl}}(\tilde{\boldsymbol{x}}^k)}{\partial \tilde{\boldsymbol{x}}} \tag{10}$$

Iterations end based on a relative error convergence criterion. In the following, quantities relating to a converged solution are highlighted by $(\star)$.

2.2 Path following: continuation

Nonlinear mechanical systems' dynamical responses often exhibit amplitude jumps during frequency sweeps. These phenomena indicate that coexisting stable solutions may exist for a given angular frequency ω. By coupling the HBM to a continuation technique [18], it becomes well-suited for the prediction of such coexisting solutions as it allows Newton's solver to overcome limit or turning points where the Jacobian matrix $\mathbf{R}_{,\tilde{\boldsymbol{x}}}$ is singular. Besides, continuation also greatly increases the robustness of Newton's solver by providing it well-chosen initial guesses. In this paper, a commonly used predictor-corrector strategy [18, 19] is considered: the arc-length continuation technique.

2.3 Computation of nonlinear contact forces

Alternating Frequency/Time scheme

In order to evaluate the residual in Eq. (5), it is necessary to determine $\tilde{\boldsymbol{f}}_{\mathrm{nl}}$. However, as it is generally not possible to have an explicit analytical expression of the nonlinear forces in Fourier domain, the Alternating Frequency/Time (AFT) scheme [20] is often used. It consists in using an inverse Discrete Fourier Transform (DFT) to translate the Fourier coefficients $\tilde{\boldsymbol{x}}$ into displacements $\boldsymbol{x}$ and velocities $\dot{\boldsymbol{x}}$ in the time domain—using N time steps over one period—in order to evaluate nonlinear forces $\boldsymbol{f}_{\mathrm{nl}}(\boldsymbol{x}, \dot{\boldsymbol{x}})$ and their partial derivatives $\boldsymbol{f}_{\mathrm{nl},\boldsymbol{x}}$, $\boldsymbol{f}_{\mathrm{nl},\dot{\boldsymbol{x}}}$ and $\boldsymbol{f}_{\mathrm{nl},\omega}$. Using a DFT, the latter may then be projected back in the frequency domain to obtain $\tilde{\boldsymbol{f}}_{\mathrm{nl}}$, $\tilde{\boldsymbol{f}}_{\mathrm{nl},\tilde{\boldsymbol{x}}}$ and $\tilde{\boldsymbol{f}}_{\mathrm{nl},\omega}$. The inverse and forward DFT may be conveniently written as linear operators so that, the rectangular $(nN \times n(2H+1))$-dimensional inverse DFT matrix reads:

$$\boldsymbol{\Gamma} = \left[\mathbf{I}_n \otimes \begin{bmatrix} 1/2 \\ \vdots \\ 1/2 \end{bmatrix} \mathbf{I}_n \otimes \begin{bmatrix} \cos(\omega t_0) \\ \vdots \\ \cos(\omega t_{N-1}) \end{bmatrix} \mathbf{I}_n \otimes \begin{bmatrix} \sin(\omega t_0) \\ \vdots \\ \sin(\omega t_{N-1}) \end{bmatrix} \dots \right.$$
$$\left. \dots \quad \mathbf{I}_n \otimes \begin{bmatrix} \cos(H\omega t_0) \\ \vdots \\ \cos(H\omega t_{N-1}) \end{bmatrix} \quad \mathbf{I}_n \otimes \begin{bmatrix} \sin(H\omega t_0) \\ \vdots \\ \sin(H\omega t_{N-1}) \end{bmatrix} \right] \tag{11}$$

and the forward DFT matrix reads:

$$\boldsymbol{\Gamma}^{-1} = \frac{2}{N} \begin{bmatrix} \mathbf{I}_n \otimes & [1 & \dots & 1] \\ \mathbf{I}_n \otimes & [\cos(\omega t_0) & \dots & \cos(\omega t_{N-1})] \\ \mathbf{I}_n \otimes & [\sin(\omega t_0) & \dots & \sin(\omega t_{N-1})] \\ & & \vdots & \\ \mathbf{I}_n \otimes & [\cos(H\omega t_0) & \dots & \cos(H\omega t_{N-1})] \\ \mathbf{I}_n \otimes & [\sin(H\omega t_0) & \dots & \sin(H\omega t_{N-1})] \end{bmatrix} \tag{12}$$

Semi-analytical computation of derivatives

The accuracy and the efficiency of the AFT procedure highly depend on N. While the Nyquist-Shanon criterion gives a theoretical lower bound value such as $N \geq 2H+1$ to prevent aliasing errors, the AFT scheme often requires a much larger number of time samples when considering nonlinearities such as structural contact [19]. The numerical accuracy of derivatives $\tilde{\boldsymbol{f}}_{\mathrm{nl},\tilde{\boldsymbol{x}}}$ and $\tilde{\boldsymbol{f}}_{\mathrm{nl},\omega}$ is then critical to ensure the robustness of the iterative solver [14]. The linearity of DFT operators $\boldsymbol{\Gamma}$ and $\boldsymbol{\Gamma}^{-1}$ along with the chain rule provide an efficient general analytic formulation of derivatives [2]:

$$\begin{aligned} \frac{\partial \tilde{\boldsymbol{f}}_{\mathrm{nl}}(\tilde{\boldsymbol{x}})}{\partial \tilde{\boldsymbol{x}}} &= \frac{\partial \tilde{\boldsymbol{f}}_{\mathrm{nl}}}{\partial \boldsymbol{f}_{\mathrm{nl}}} \frac{\partial \boldsymbol{f}_{\mathrm{nl}}}{\partial \boldsymbol{x}} \frac{\partial \boldsymbol{x}}{\partial \tilde{\boldsymbol{x}}} + \frac{\partial \tilde{\boldsymbol{f}}_{\mathrm{nl}}}{\partial \boldsymbol{f}_{\mathrm{nl}}} \frac{\partial \boldsymbol{f}_{\mathrm{nl}}}{\partial \dot{\boldsymbol{x}}} \frac{\partial \dot{\boldsymbol{x}}}{\partial \tilde{\boldsymbol{x}}} \\ &= \boldsymbol{\Gamma}^{-1} \frac{\partial \hat{\boldsymbol{f}}_{\mathrm{nl}}}{\partial \boldsymbol{x}} \boldsymbol{\Gamma} + \boldsymbol{\Gamma}^{-1} \frac{\partial \hat{\boldsymbol{f}}_{\mathrm{nl}}}{\partial \dot{\boldsymbol{x}}} \boldsymbol{\Gamma} (\omega \boldsymbol{\nabla} \otimes \mathbf{I}_n) \end{aligned} \tag{13}$$

where the $(nN \times nN)$ matrices of partial derivatives of $\boldsymbol{f}_{\text{nl}}$ evaluated at N time steps[1] are defined by:

$$\begin{aligned}
\frac{\partial \hat{\boldsymbol{f}}_{\text{nl}}}{\partial \boldsymbol{x}} &= \alpha \begin{bmatrix} \operatorname{diag}\left(\frac{\partial \boldsymbol{f}_1}{\partial \boldsymbol{x}_1}\right) & \dots & \operatorname{diag}\left(\frac{\partial \boldsymbol{f}_1}{\partial \boldsymbol{x}_n}\right) \\ \vdots & \ddots & \vdots \\ \operatorname{diag}\left(\frac{\partial \boldsymbol{f}_n}{\partial \boldsymbol{x}_1}\right) & \dots & \operatorname{diag}\left(\frac{\partial \boldsymbol{f}_n}{\partial \boldsymbol{x}_n}\right) \end{bmatrix} \\
\frac{\partial \hat{\boldsymbol{f}}_{\text{nl}}}{\partial \dot{\boldsymbol{x}}} &= \frac{\alpha}{\beta} \begin{bmatrix} \operatorname{diag}\left(\frac{\partial \boldsymbol{f}_1}{\partial \dot{\boldsymbol{x}}_1}\right) & \dots & \operatorname{diag}\left(\frac{\partial \boldsymbol{f}_1}{\partial \dot{\boldsymbol{x}}_n}\right) \\ \vdots & \ddots & \vdots \\ \operatorname{diag}\left(\frac{\partial \boldsymbol{f}_n}{\partial \dot{\boldsymbol{x}}_1}\right) & \dots & \operatorname{diag}\left(\frac{\partial \boldsymbol{f}_n}{\partial \dot{\boldsymbol{x}}_n}\right) \end{bmatrix}
\end{aligned} \tag{14}$$

and where:

$$\begin{aligned}
\frac{\partial \tilde{\boldsymbol{f}}_{\text{nl}}(\tilde{\boldsymbol{x}}, \omega)}{\partial \omega} &= \frac{\partial \tilde{\boldsymbol{f}}_{\text{nl}}}{\partial \boldsymbol{f}_{\text{nl}}} \beta \frac{\partial \boldsymbol{f}_{\text{nl}}}{\partial \omega} + \frac{\partial \tilde{\boldsymbol{f}}_{\text{nl}}}{\partial \boldsymbol{f}_{\text{nl}}} \frac{\partial \boldsymbol{f}_{\text{nl}}}{\partial \dot{\boldsymbol{x}}} \frac{\partial \dot{\boldsymbol{x}}}{\partial \omega} \\
&= \boldsymbol{\Gamma}^{-1} \beta \frac{\partial \boldsymbol{f}_{\text{nl}}}{\partial \omega} + \boldsymbol{\Gamma}^{-1} \frac{\partial \hat{\boldsymbol{f}}_{\text{nl}}}{\partial \dot{\boldsymbol{x}}} \boldsymbol{\Gamma} (\boldsymbol{\nabla} \otimes \mathbf{I}_n) \tilde{\boldsymbol{x}}
\end{aligned} \tag{15}$$

The AFT scheme usually relies on Fast Fourier Transforms (FFT). Using real input FFT algorithms that exploit the spectrum's symmetry of real-valued sequences increases numerical performances. It also significantly enhances the accuracy of the Jacobian matrix $\partial \tilde{\boldsymbol{f}}_{\text{nl}} / \partial \tilde{\boldsymbol{x}}$.

2.4 Nonlinear condensation

When considering large industrial systems featuring nonlinear interfaces, it is common practice to distinguish linear and nonlinear dof. This yields a reorganization [21] of Eq. (5) which leads to significant gains in terms of computational efficiency.

2.5 Regularization of contact forces

Blade-tip/casing contact forces are generally expressed in a cylindrical coordinate system (r, θ, z). Their computation follow the evaluation of the gap function $\boldsymbol{g}(t)$ defined as the signed distance between contact nodes and the casing:

$$g_{j,i} = x_{3j-2,i} - d_{j,i} \quad \text{for } j \in [\![1..n_{\text{b}}]\!],\ i \in [\![0..N-1]\!] \tag{16}$$

where x_{3j-2} is the radial displacement of the j-th contact node, $d_{j,i}$ the radial position of the casing and n_{b} is the number of contact nodes so that:

$$\begin{aligned}
\boldsymbol{g} &= [\boldsymbol{g}_1, \dots, \boldsymbol{g}_{n_{\text{b}}}]^\top \\
&= [g_{1,0}, \dots, g_{1,N-1}, \dots, g_{n_{\text{b}},0}, \dots, g_{n_{\text{b}},N-1}]^\top
\end{aligned} \tag{17}$$

In the RL-HBM framework, radial components of the contact forces are evaluated by means of a regularized penalty law:

$$f_{3j-2,i} = \kappa \frac{g_{j,i}}{2} + \sqrt{\left(\kappa \frac{g_{j,i}}{2}\right)^2 + \gamma^2} \tag{18}$$

where $\kappa \in \mathbb{R}_+$ is the penalty coefficient and $\gamma \in \mathbb{R}_+$ is a smoothing coefficient. To better visualize the impact of such a regularization, regularized normal force-displacement relationship is compared to the classically used contact laws in Fig. 1.

[1] These may be seen as Jacobian matrices diagonally extended to contain all evaluated time samples over one period of motion.

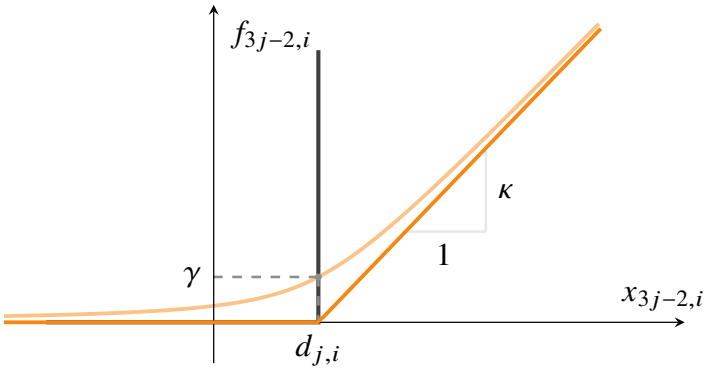

Figure 1 – Contact laws: penalty (—), regularized penalty (—) and unilateral contact (—) as functions of one of the radial displacement components.

Taking dry friction into account through the Coulomb law implies that the contact force has a circumferential component:

$$f_{3j-1,i} = \mu \frac{\dot{x}_{3j-1,i} + r_j\omega}{\sqrt{\left(\dot{x}_{3j-1,i} + r_j\omega\right)^2 + \dot{x}_{3j,i}^2}} f_{3j-2,i} = \mu_{3j-1,i} f_{3j-2,i} \tag{19}$$

as well as an axial component:

$$f_{3j,i} = \mu \frac{\dot{x}_{3j,i}}{\sqrt{\left(\dot{x}_{3j-1,i} + r_j\omega\right)^2 + \dot{x}_{3j,i}^2}} f_{3j-2,i} = \mu_{3j,i} f_{3j-2,i} \tag{20}$$

where μ is the friction coefficient with $\sqrt{\mu_{3j-1,i}^2 + \mu_{3j,i}^2} = \mu$, and $\dot{x}_{3j-1,i}$, $\dot{x}_{3j,i}$ and r_j are respectively the tangential velocity, the axial velocity and the radial position of the j-th contact node. Because of the very high relative speed between the blade-tip and the inner surface of the casing, permanent sliding is assumed at all time.

2.6 Lanczos filtering

Filtering of the contact forces is performed through a Lanczos σ-approximation. This is key to mitigate spurious oscillations associated to the Gibbs phenomenon and reduces aliasing errors induced by the AFT scheme. Filtering is achieved by directly applying some decaying multiplicative factors in Fourier domain to the contact forces obtained at the end of an AFT cycle, so that:

$$\boldsymbol{f}_{\mathrm{nl}}(\boldsymbol{x}, \dot{\boldsymbol{x}}, \omega) \simeq \frac{1}{2}\boldsymbol{a}_0^{\mathrm{nl}} + \sum_{j=1}^{H} \sigma_j \left[\boldsymbol{a}_j^{\mathrm{nl}} \cos\left(j\omega t\right) + \boldsymbol{b}_j^{\mathrm{nl}} \sin\left(j\omega t\right)\right] \tag{21}$$

where:

$$\sigma_j = \mathrm{sinc}(\mathcal{X}_j)^m \quad \text{with} \quad \mathcal{X}_j = \begin{cases} 0 & \text{for } j < 1 \\ \frac{j}{H+1} & \text{for } 1 \leq j \leq H \end{cases} \tag{22}$$

where $m \in \mathbb{R}_+$ is the smoothing exponent. For $m = 0$, contact forces are not filtered.

3 Stability analysis

The stability analysis of computed solutions, based on Floquet theory, and the detection of bifurcations [22] are key to obtain a qualitative understanding of blade-tip/casing interactions.

3.1 Time domain

In the time domain, the assessment of the stability of a solution $\boldsymbol{x}^\star$ relies on the computation of the monodromy matrix $\mathcal{M}$ [14, 15]. Computing $\mathcal{M}$ is numerically challenging as a compromise must be found between a high level of accuracy that is needed for relevant results and computational efficiency. In this paper, we use the $2n$-pass algorithm [15] in which $\mathcal{M}$ is evaluated by integrating $2n$ times over one period T the linear system:

$$\frac{\alpha}{\beta^2}\mathbf{M}\ddot{\boldsymbol{x}}(t) + \frac{\alpha}{\beta}\left[\mathbf{C} + \left.\frac{\partial \boldsymbol{f}_{\text{nl}}^\star}{\partial \dot{\boldsymbol{x}}}\right|_{t=\tau_i}\right]\dot{\boldsymbol{x}}(t) + \beta\left[\mathbf{K} + \left.\frac{\partial \boldsymbol{f}_{\text{nl}}^\star}{\partial \boldsymbol{x}}\right|_{t=\tau_i}\right]\boldsymbol{x}(t) = \mathbf{0} \tag{23}$$

A set of $2n$ linearly independent initial conditions stacked in $\boldsymbol{z}^{(k)}(t_0) = [\boldsymbol{x}(t_0),\, \dot{\boldsymbol{x}}(t_0)]^\top$ with $k \in [\![1..2n]\!]$ at $t_0 = 0$ are considered. In practice, these initial conditions correspond to the columns of the identity matrix $\mathbf{I}_{2n}$. The state space Jacobian matrices of the nonlinear forces at each instant are obtained as a by-product of the AFT cycle associated to the converged solution. The monodromy matrix may thus be constructed as a concatenation of the resulting state vectors obtained at $t_N = T$:

$$\mathcal{M} = \left[\ \boldsymbol{z}^{(1)}(T),\ \ldots,\ \boldsymbol{z}^{(k)}(T),\ \ldots,\ \boldsymbol{z}^{(2n)}(T)\ \right] \tag{24}$$

The eigenvalues of $\mathcal{M}$ are called the Floquet multipliers, denoted ρ_m in the following. They are unique and linked to the Floquet exponents α_m by the following relations:

$$\rho_m = \mathrm{e}^{\alpha_m T} \Leftrightarrow \alpha_m = \frac{1}{T}\ln(|\rho_m|) + \mathrm{i}\frac{\arg(\rho_m) + 2k\pi}{T},\ k \in \mathbb{Z} \tag{25}$$

For a given $\boldsymbol{x}^\star$, should one of the Floquet multipliers have a modulus greater than one, or, equivalently, one of the Floquet exponents have a positive real part, then the solution would be unstable. Otherwise, it is considered stable. The implicit Newmark scheme of average acceleration is used to integrate Eq. (23) as it is advantageously unconditionally stable for linear systems. This method is referred to as the Newmark $2n$-pass method in the following.

3.2 Frequency domain

In order to evaluate the stability of a periodic solution in the frequency domain, the same procedure as described in [18, 16] is applied to the equation of motion. It yields the following quadratic eigenvalue problem:

$$(\mathbf{R}_{,\tilde{\boldsymbol{x}}}^\star + \boldsymbol{\Delta}_1 s + \boldsymbol{\Delta}_2 s^2)\mathbf{q} = \mathbf{0} \tag{26}$$

where $(s, \mathbf{q})$ are the complex eigensolutions and where the terms $\boldsymbol{\Delta}_1$ and $\boldsymbol{\Delta}_2$ are given by:

$$\begin{aligned}
\boldsymbol{\Delta}_1 &= 2\omega^\star \boldsymbol{\nabla} \otimes \frac{\alpha}{\beta^2}\mathbf{M} + \mathbf{I}_{2H+1} \otimes \frac{\alpha}{\beta}\mathbf{C} + \hat{\mathbf{C}} \quad \text{with} \quad \hat{\mathbf{C}} = \boldsymbol{\Gamma}^{-1}\frac{\partial \hat{\boldsymbol{f}}_{\text{nl}}^\star}{\partial \dot{\boldsymbol{x}}}\boldsymbol{\Gamma} \\
\boldsymbol{\Delta}_2 &= \mathbf{I}_{2H+1} \otimes \frac{\alpha}{\beta^2}\mathbf{M}
\end{aligned} \tag{27}$$

where $\boldsymbol{\nabla}$ is given by Eq. (7). In the case where nonlinear forces explicitly depend on velocities, $\hat{\mathbf{C}}$ has to be evaluated separately [12, 13]. In order to be solved, Eq. (26) must be recast into an equivalent generalized eigenvalue problem of double size using a first companion form linearization:

$$\begin{bmatrix} \mathbf{0}_{n_H} & \mathbf{I}_{n_H} \\ -\mathbf{R}_{,\tilde{\boldsymbol{x}}}^\star & -\boldsymbol{\Delta}_1 \end{bmatrix}\bar{\mathbf{q}} = s\begin{bmatrix} \mathbf{I}_{n_H} & \mathbf{0}_{n_H} \\ \mathbf{0}_{n_H} & \boldsymbol{\Delta}_2 \end{bmatrix}\bar{\mathbf{q}} \quad \text{with} \quad \bar{\mathbf{q}} = \begin{bmatrix} \mathbf{q} \\ s\mathbf{q} \end{bmatrix} \tag{28}$$

or, in a more compact eigendecomposition form:

$$(\mathcal{H} - s\,\mathbf{I}_{2n_H})\,\bar{\mathbf{q}} = \mathbf{0} \quad \text{with} \quad \mathcal{H} = \begin{bmatrix} \mathbf{0}_{n_H} & \mathbf{I}_{n_H} \\ -\boldsymbol{\Delta}_2^{-1}\mathbf{R}_{,\tilde{\boldsymbol{x}}}^\star & -\boldsymbol{\Delta}_2^{-1}\boldsymbol{\Delta}_1 \end{bmatrix} \tag{29}$$

Solving Eq. (29) yields the Hill's coefficients $\boldsymbol{s}$ defined as the $2n(2H+1)$ complex eigenvalues of $\mathcal{H}$.

In theory, the $2n(2H+1)$ eigenvalues are clustered in $2H+1$ families of $2n$ eigenvalues having the same real parts and imaginary parts shifted by integer multiples of ω. However, this structure is broken by the harmonic truncation. That is why, among the full set of coefficients $\boldsymbol{s}$, there only exists $2n$ eigenvalues that approximate the Floquet exponents α_m. The selection of these $2n$ eigenvalues relies on specific sorting algorithms that may be divided in three categories: (1) eigenvalue sorting [23, 16], (2) spectral primitive cell sorting [24] (see theorem 3), and (3) eigenvector sorting [25, 10]. For high dimension mechanical systems, it was found that Hill's spectrum will not necessarily be sufficiently converged to successfully apply the spectral primitive cell sorting algorithm. Also, eigenvector sorting has not been considered as it should be applied on the full raw Hill's spectrum [10]. Hence, only the eigenvalue sorting algorithm is considered in the remainder. For the sake of numerical efficiency, only a subset of Hill's spectrum—the $4n$ eigenvalues with lowest magnitudes—is computed.

4 NASA rotor 37

Rotor 37 is a 36-blade transonic axial compressor stage that was designed at NASA's Lewis research center in the late 1970s [26, 27]. It is an open geometry extensively used in aerodynamic investigations, and served as a benchmark in the field of Computed Fluid Dynamics. More recently, it has been employed as an reference test case for the analysis of blade-tip/casing contact interactions in both time [7] and frequency [8, 9] domains.

The numerical model used in this paper is identical to the one used in previous works [8, 9]. Rotor 37 is made of a nickel-based alloy, the mechanical properties of a 18-Ni 200-maraging alloy are here considered for the numerical simulations: Young's modulus $E = 180$ GPa, density $\rho = 8000$ kg·m^{-3} and Poisson's ratio $\nu = 0.3$. The 3D finite element mesh of the blade comprises 1800 quadratic hexahedral elements with a total of 5745 nodes. The root of the blade is clamped. For numerical efficiency reasons, a reduced-order model is computed with the Craig-Bampton method [28]. The nonlinear interface features $n_\mathrm{b} = 8$ nodes evenly spaced along the blade-tip. The resulting reduced order model contains 24 physical dof and $\eta = 10$ modal dof. Convergence of the blade eigenfrequencies for the first five free vibration modes with respect to the mesh discretization and the reduction parameter η has been checked but is not detailed here for the sake of brevity. Modal damping is assumed with a coefficient $\xi_{1-2} = 1 \cdot 10^{-3}$ for the first bending and torsional modes, and $\xi_{3+} = 5 \cdot 10^{-3}$ for all other modes.

5 Numerical results

In total, four distinct configurations are considered in this section. The whole methodology—including the application of the RL-HBM and stability analyses—is first applied with (1) cubic springs in the tangential direction for each contact node. The severity of the nonlinearity is then progressively increased considering (2) unilateral contact constraints on a perfectly circular rigid casing, (3) unilateral contact constraints on a deformed rigid casing, and (4) unilateral contact constraints on a deformed rigid casing accounting for centrifugal effects. For the first two configurations only, an external forcing is imposed on the blade.

5.1 Cubic nonlinearity

While the blade model is different, the configuration of interest is inspired from the literature [12]. It is used as a test case to verify the implementation of the stability assessment algorithms. Nonlinear smooth cubic springs are considered in the tangential direction of each node in the blade's contact interface, see Fig. 2. Nonlinear forces components are expressed as:

$$f_{3j-1,i} = \alpha_\theta \, x_{j-1,i}^3 \quad \text{for } j \in [\![1..n_\mathrm{b}]\!],\ i \in [\![0..N-1]\!] \tag{30}$$

with $\alpha_\theta = 1 \cdot 10^9$ N·m^{-3}. An external forcing related along the blade's first bending mode ($\omega_{1\mathrm{B}} = 5272.3$ rad·s^{-1}) is considered:

$$\boldsymbol{f}_\mathrm{ext}(t,\omega) = \bar{f}_\mathrm{ext} \mathbf{M} \boldsymbol{\phi}_{1\mathrm{B}} \cos(\omega t) \tag{31}$$

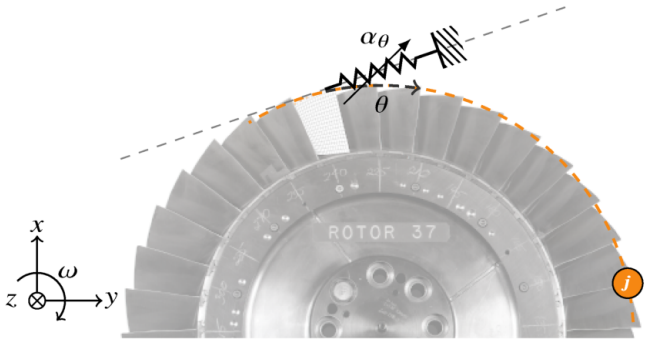

Figure 2 – Configuration with a cubic nonlinearity, trajectory of the j-th contact node (●).

where $\bar{f}_{\text{ext}} = 125$ N is the forcing amplitude and $\boldsymbol{\phi}_{1\text{B}}$ is the eigenvector corresponding to the first bending mode.

The Nonlinear Frequency Response Curve (NFRC) related to the blade's leading edge radial displacements r_1, obtained for $H = 40$ and $N = 2048$ is depicted in Fig. 3a.

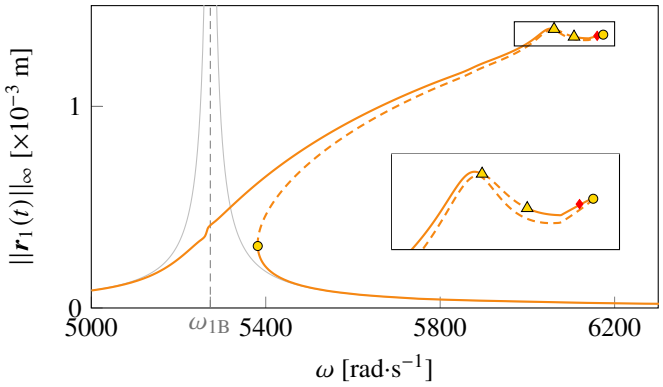

(a) Linear forced response function (—) and nonlinear frequency response curve, stable (—) and unstable (- - -) solutions

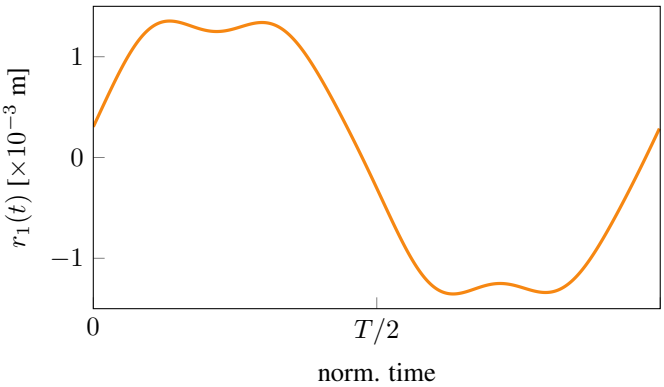

(b) Time response at the nonlinear resonance (♦)

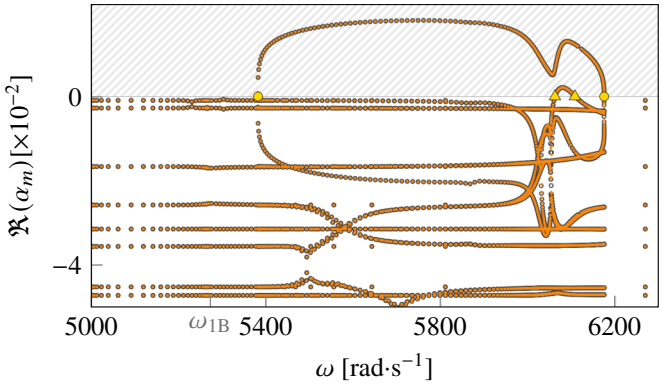

(c) Real part of Floquet exponents (○), selected Hill coefficients (●)

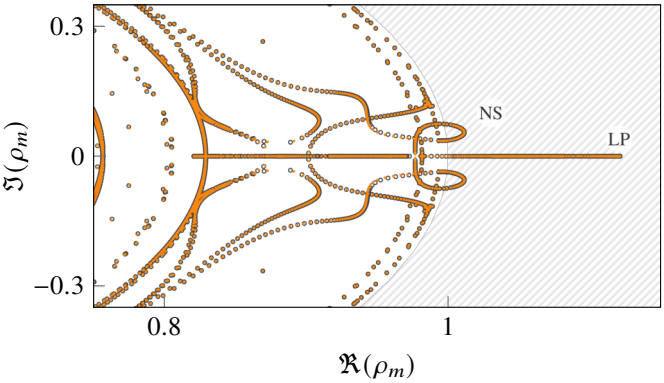

(d) Floquet (○) and selected Hill (●) multipliers, zoom on $1 + 0\text{i}$

Figure 3 – Blade response with a cubic nonlinearity, comparison of stability assessment in time and frequency domains for a cubic nonlinearity.

The time response corresponding to the nonlinear resonance (♦) is plotted in Fig. 3b. Stability assessment is performed in both time and frequency domains. The real part of the $2n = 68$ Floquet exponents resulting from the monodromy matrix and selected Hill coefficients as functions of the angular frequency ω are shown in Fig. 3c.

As a reminder, a solution is assumed unstable when one of the associated Floquet multipliers has a modulus greater than one or, equivalently, when the real part of one of the Floquet exponents is positive, which corresponds to the hatched area in Fig. 3c (▨). With respect to the different types of bifurcations, these may be assessed in the complex plane. A zoom of the latter around the value $1 + 0\mathrm{i}$ is depicted in Fig. 3d.

Limit points (●) (LP), which are detected when a Floquet exponent leaves the unit circle through the point $1 + 0\mathrm{i}$, are static bifurcations corresponding to a singularity of the Jacobian $\mathbf{R}^{\star}_{,\tilde{\boldsymbol{x}}}$. They are characterized by a vertical tangent on the NFRC. In addition, two Neimark-Sacker (▲) (NS) bifurcations, which are identified when a pair of Floquet multipliers crosses the unit circle as complex conjugates, marks a new emanating branch of either quasiperiodic or periodic solutions depending on the absolute value of the imaginary part of the corresponding exponents.

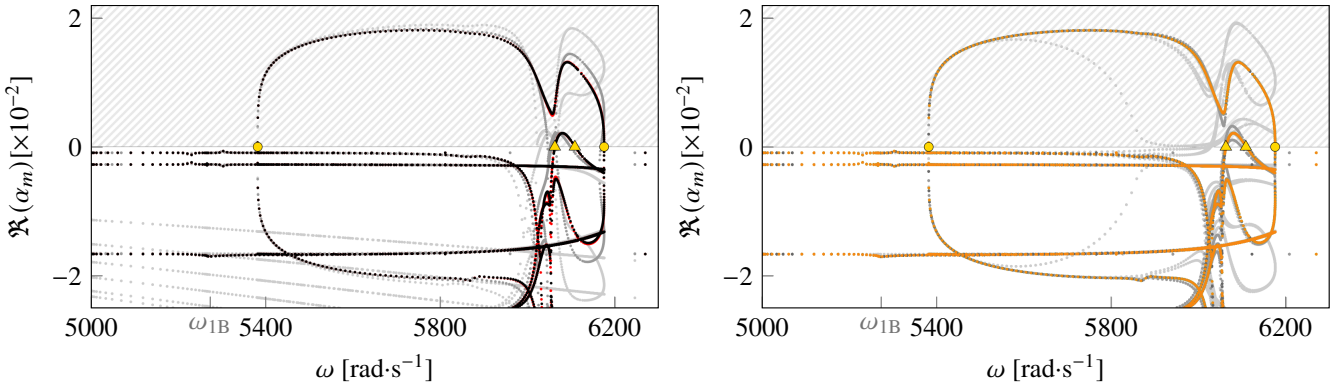

(a) Real part of Floquet exponents for $N = \{128(●), 256(●), 1024(●)\}$ for $H = 20$ and $H, N = \{40, 2048\}(●)$

(b) Real part of selected Hill coefficients for $H = \{5(●), 8(●)\}$, $10(●)$, $20(●)\}$ for $N = 1024$ and $H, N = \{40, 2048\}(●)$

Figure 4 – Convergence of the Newmark $2n$-pass method and Hill's method.

Looking at both Figs. 3c and 3d, there is a perfect agreement between the results of the stability analysis conducted with the monodromy matrix and Hill's method. This result underlines that for cubic nonlinearities, both methodologies may be employed in a computationally efficient manner.

In order to appreciate the influence of the values of H and N, on the results obtained with the Newmark $2n$-pass method and Hill's method, results obtained for several values of these parameters are plotted in Fig. 4. For the sake of brevity, convergence of each method is shown with respect to the numerical parameter to which it was found to be most sensitive: N for the Newmark $2n$-pass method, and H for Hill's method. A close look at each set of results underlines that $H = 10$ already yields converged results for Hill's method while at least $N = 1024$ time steps are required to reach convergence with the Newmark $2n$-pass method. For both methods, it is found that results are perfectly converged for $N = 1024$ and $H = 20$, they cannot be distinguished from those obtained with for $N = 2048$ and $H = 40$.

It was observed, yet not shown here for the sake of conciseness, that Hill's method appears less sensitive to N than the Newmark $2n$-pass method and converges faster [25].

Overall, there is an excellent agreement between the Floquet exponents computed with the Newmark $2n$-pass method and the ones obtained with Hill's method.

5.2 Contact on a circular casing

In this second test case, a perfectly circular rigid casing is considered around the blade. From a numerical standpoint, this circular casing is implemented as a fixed gap facing the blade-tip as it rotates. Consequently, the relative

distance coordinates $d_{j,i}$ from Eq. (16) thus read:

$$d_{j,i} = c_j \tag{32}$$

where c_j represents the nominal blade-tip/casing clearance in front of the j-th contact node, see Fig. 5. It is here assumed that $c_j = 5 \cdot 10^{-4}$ m for all contact nodes. Contact is initiated by means of an external forcing applied on the blade, similarly to Eq. (31) with $\bar{f}_{\text{ext}} = 150$ N. The frequency range of excitation surrounds the first eigenfrequency ω_{1B} of the blade.

For this configuration as well as the other ones considered in the rest of the paper, normal contact forces are computed with the regularized penalty law given in Eq. (18) considering $\kappa = 1 \cdot 10^9$ N·m^{-1} and $\gamma = 6 \cdot 10^2$ N. Coulomb friction forces are accounted for with a friction coefficient $\mu = 0.15$ through Eqs. (19) and (20). In the end, the dimension of the nonlinear partition corresponds to the number of nonlinear dof: $3n_{\text{b}} = 24$.

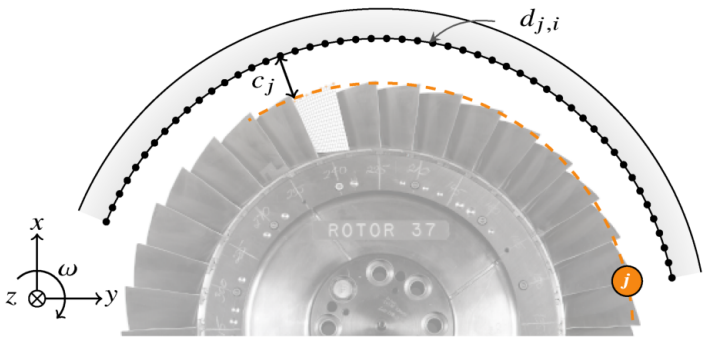

Figure 5 – Configuration with a circular casing.

The NFRC of the blade's leading edge radial displacement r_1 is depicted in Fig. 6a. The value of the associated numerical parameters ($H = 80$, $N = 2048$ and a Lanczos filter considering $m = 1$) results from a convergence analysis not detailed here for the sake of brevity. The fixed gap is indicated (——) on the figure as it defines the vibration amplitude for which the system becomes nonlinear. Also, the radial displacement of the leading edge over one period close to the nonlinear resonance (♦) is plotted in Fig. 6b. One may note that there is no significant residual penetration of the blade within the casing, thus confirming *a posteriori* the parameters of the regularized contact law.

For each solution, the real part of the Floquet exponents is presented in Fig. 7, they are obtained with the Newmark $2n$-pass method and Hill's method for several values of H and N. In comparison to the results obtained with a cubic nonlinearity, the results pictured in Fig. 7 underline the intricacy of the blade's dynamics as it undergoes contact constraints. Indeed, two limit points (●) are predicted along with four Neimark-Sacker (▲) bifurcations on the branch of higher amplitude. In addition, these results also underline an increased numerical sensitivity of both stability assessment methodology. In particular, one may observe that results obtained with the Newmark $2n$-pass method converge very slowly towards those of Hill's method. While it has been checked that results obtained with Hill's method for $H = 80$ and $N = 2048$ are converged, the Newmark $2n$-pass method requires significantly higher values of each of these parameters to converge, thus implying a significant increase in computational complexity.

In addition, the slow convergence of the Newmark $2n$-pass method prevents an accurate prediction of bifurcations contrary to what is observed with Hill's method. As a matter of fact, for $H = 80$ and $N = 2048$, the predicted bifurcations (see the symbols (●) and (▲) in Fig. 7) are in good agreement with the NFRC, see Fig. 6a.

Observations made with respect to the good numerical behaviour of Hill's method, and its ability to provide accurate results for small values of H and N may go against previous observations [15, 11]. Indeed, while there is a consensus on the fact that nonsmooth nonlinearities theoretically prevent the application of Hill's method (and more generally the Floquet framework), the regularization of the contact law considered in the RL-HBM may explain why Hill's method can here be successfully applied. In addition, it is found that the numerical specificities of the RL-HBM,

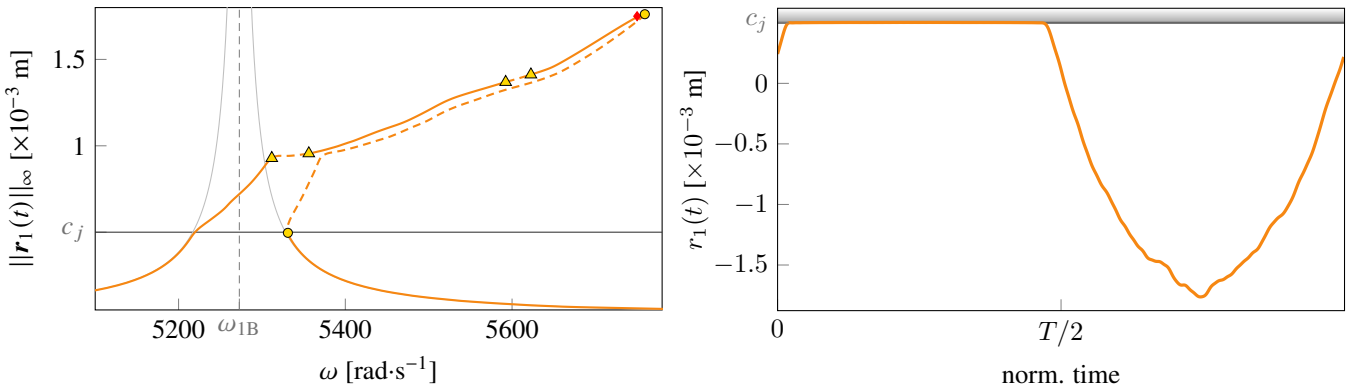

(a) Linear forced response function (—) and nonlinear frequency response curve, stable (—) and unstable (- - -) solutions

(b) Time response at the nonlinear resonance (♦)

Figure 6 – Blade response with a perfectly circular casing.

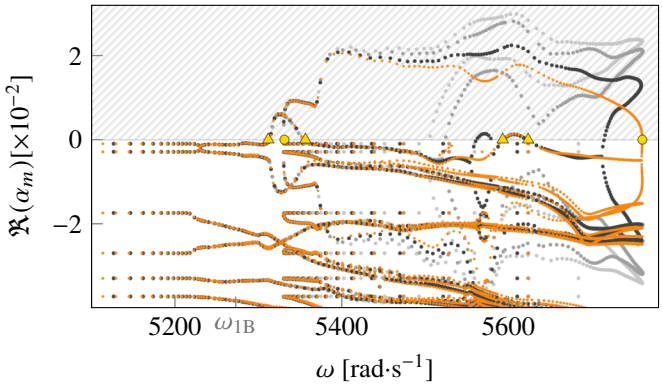

Figure 7 – Real part of Floquet exponents $H, N = \{40, 1024\}$(●); $\{50, 2048\}$(●); $\{80, 2048\}$(●), selected Hill coefficients $H, N = \{80, 2048\}$(●).

including Lanczos filtering and the semi-analytical computation of derivatives, alleviates numerical challenges so that Hill's method may be applied efficiently. Finally, it has also been observed that a careful application of sorting algorithms is essential to avoid numerical artifacts.

5.3 Contact on a deformed casing

In this third configuration, blade-tip/casing contacts are initiated by the deformation of the casing. From a numerical standpoint, this configuration is thus significantly more sensitive than the previous one since there is no linear solution over the considered frequency range anymore. Numerically, the deformed casing is implemented by means of a variable obstacle position, depending on the blade angular position. Components $d_{j,i}$ of Eq. (16) are now evaluated as follows [8, 9]:

$$d_{j,i} = c_j - (c_j + p_j) \exp\left[-\left(\frac{(\tau_i + \theta_j) \pmod{2\pi/n_l} - \pi/n_l}{w_l} \right)^2 \right] \tag{33}$$

where, n_l is the number of lobes, w_l the angular width of the contact areas, θ_j the initial angular location of contact node j, c_j the operating clearance and p_j the penetration of the casing profile with respect to the trajectory of contact node j when the blade does not vibrate (- - -). The casing is assumed to be distorted in such a way that

there are two symmetrical privileged contact areas along its inner circumference. The following values are considered in the remainder: $n_l = 2$, $w_l = 0.15$, and $\forall j$, $c_j = 5 \cdot 10^{-4}$ m and $p_j = 1.25 \cdot 10^{-4}$ m. A partial view of the considered casing featuring one of the two lobes may be seen in Fig. 8. Finally, there is no external forcing applied on the blade: $\boldsymbol{f}_{\text{ext}}(\omega, t) = \mathbf{0}$.

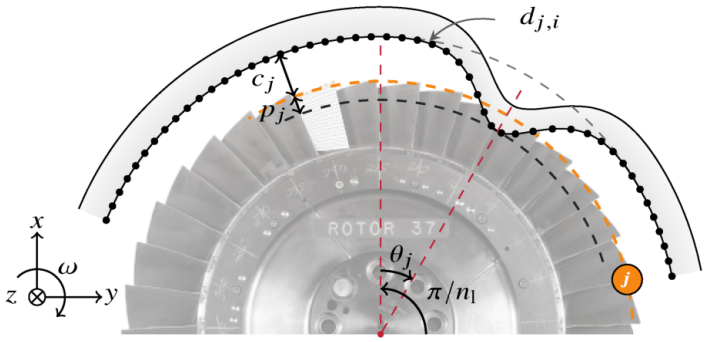

Figure 8 – Configuration with a deformed casing in front of the j-th boundary node (●).

Without forcing, the excitation of the system is related to contact only which means that the pulsation ω now relates to the blade's angular speed. For that reason, considered values of ω are smaller than in the previous configurations: $\omega \in [1250,\ 1550]$ rad·s^{-1} which includes the crossing between the blade's first bending mode and the fourth engine order [8].

5.3.1 Results without centrifugal effects

The NFRC of the blade's leading edge radial displacement r_1 is depicted in Fig. 9a. The value of the associated numerical parameters remain $H = 80$, $N = 2048$ and a $m = 1$ Lanczos filter. In order to assess the relevance of the obtained solutions, the NFRC obtained from a reference time domain solution method (×) is added in the background of the same figure[2]. Where the predicted solutions are stable and periodic, only very minor differences are observed despite of the fact that time and frequency methods rely on distinct contact treatment algorithms (Lagrange multipliers are computed in the time domain while the regularized contact law is used with the RL-HBM). Also, the radial displacement of blade's leading edge at the nonlinear resonance is plotted in Fig. 9b. Once again, one may check that residual penetrations theoretically allowed by the regularized contact law are negligible. As it was evidenced in a previous publication [9], there is an excellent agreement between the RL-HBM and time integration.

Here again, both the Newmark $2n$-pass method and Hill's method are considered for stability assessment of the solutions. Real parts of the computed Floquet exponents and Hill's coefficients are depicted in Fig. 10. The bifurcations predicted by Hill's method (symbols (●) and (▲) in Figs. 9a, 10a and 10b) for $N = 2048$ and $H = 80$ are consistent with the NFRC. They are also in good agreement with time integration results since the two Neimark-Sacker bifurcations surround an area where solutions were found to feature a sophisticated frequency content [9].

Similarly to what was observed in the previous section with a perfectly circular casing, the Newmark $2n$-pass method is found to be much more sensitive to the employed numerical parameters. For $H = 80$ and $N = 2048$, the obtained results are not converged and do not allow for an accurate assessment of the solutions' stability, as evidenced by the discrepancies between Hill's method predicted bifurcations and the location of the real part of Floquet exponents in Fig. 10a. Contrary to the perfectly circular casing configuration, the fundamental harmonics is here 2ω due to the fact that two symmetric contact lobes on the casing. Accordingly, the blade's response is essentially located on even harmonics. Since the value of $H = 80$ is kept identical for the circular casing and deformed casing configurations, there is actually a reduction of the number of relevant harmonics in the present

[2]Maximum amplitudes resulting from time integration (×) were evaluated on the last revolution of the blade over a total of 230 computed revolutions starting from null initial conditions and using a time step $h = 10^{-7}$ s.

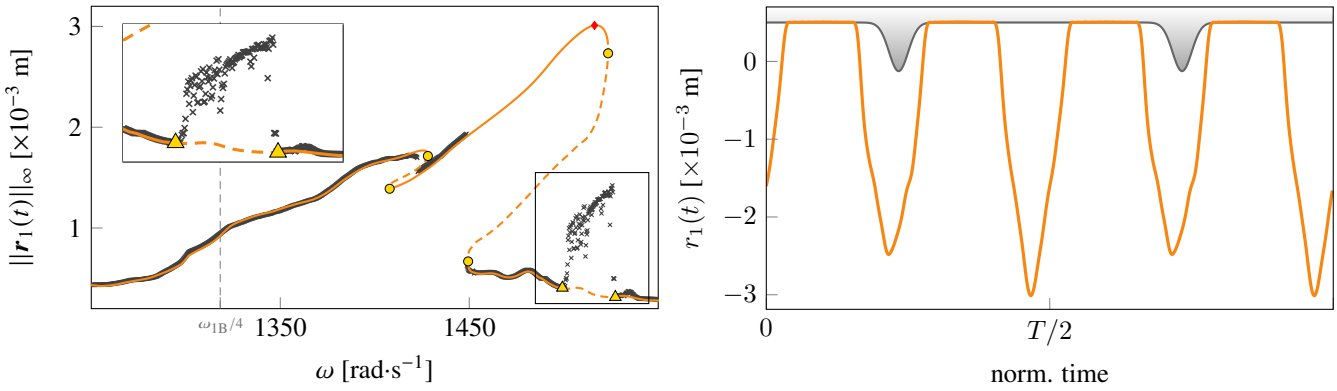

(a) Nonlinear frequency response curve, stable (—) and unstable (- - -) solutions, time integration (×)

(b) Time response at the nonlinear resonance (♦)

Figure 9 – Blade response with a deformed casing.

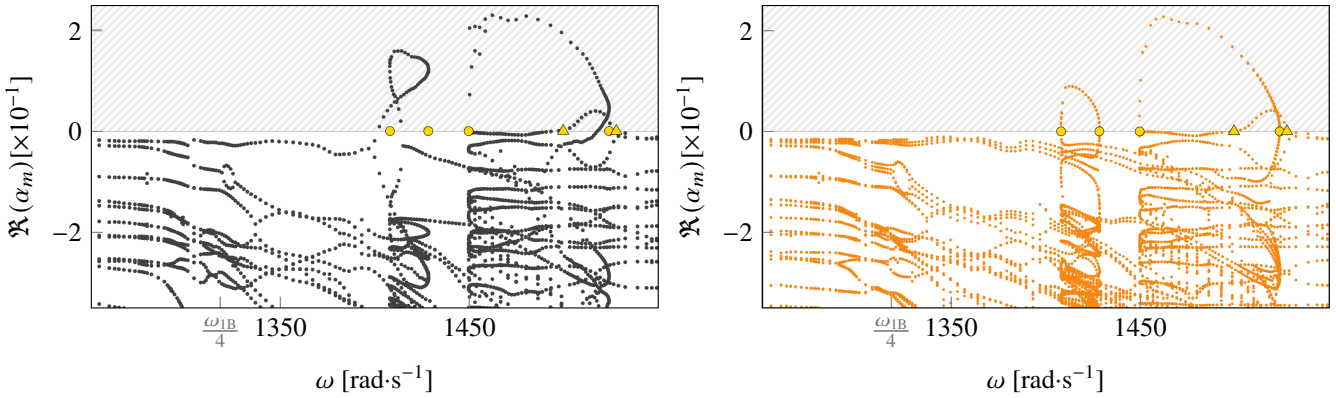

(a) Real part of Floquet exponents

(b) Real part of selected Hill's coefficients

Figure 10 – Application of the $2n$-pass method and Hill's method to the deformed casing contact configuration ($H = 80$, $N = 2048$).

configuration (40 even harmonics instead of the full 80 harmonics). It is assumed that this observation is the key to understanding why the convergence of the $2n$-pass method is even lower for the present contact configuration.

While it is not detailed here for the sake of brevity, it is also observed that the convergence of the results obtained with Hill's method and eigenvalue sorting is significantly slower for this contact configuration. However and contrary to what is observed for the Newmark $2n$-pass method, it is found that this slower convergence does not alter, or at least to a lesser extent, the accuracy of the stability assessment. When considering the full spectrum of eigenvalues, it was also numerically checked that this slower convergence was not related to the computation of an inadequate eigenvalues' subset. Same as for the Newmark $2n$-pass method, it seems likely that this slower convergence relates to the fact that the blade's dynamics is dominated by even harmonics only. Still, even with a partially accurate eigenvalue sorting, which may be seen as some Floquet exponents appear to be most likely duplicates, Hill's method still provides the critical exponents that feature larger real part values with a faster convergence rate than the Newmark $2n$-pass method. As a result, Hill's method appears as a suitable alternative to obtain a qualitative stability assessment of an industrial blade undergoing severe contact interactions.

5.3.2 Results with centrifugal effects

Centrifugal effects are now accounted for in order to increase the fidelity of the blade model. Centrifugal effects have two main implications: (1) the stiffness of the blade and (2) the blade-tip/casing clearance configuration become dependent on the angular speed ω. In this work, it is assumed that centrifugal effects only yields a dependence of the blade's stiffness matrix on the angular speed ω. As a matter of fact, while accouting for an angular speed dependent clearance configuration would be straightforward with the RL-HBM, it would blur the analysis of the results and is thus neglected in this study.

When accounting for centrifugal effects over the angular speed range $\omega \in [0,\ \omega_{\max}]$, it has been shown [29] that the blade's stiffness matrix may be written as follows:

$$\mathbf{K}(\omega) = \mathbf{K}_0 + \mathbf{K}_1\omega^2 + \mathbf{K}_2\omega^4 \tag{34}$$

where the matrices $\mathbf{K}_0$, $\mathbf{K}_1$ and $\mathbf{K}_2$ are linear combinations of stiffness matrices computed at $\omega = 0$, $\omega = \omega_{\max}/2$ and $\omega = \omega_{\max}$. Numerically, accounting for centrifugal effects implies a larger reduction basis when building the reduced-order model which now features $n = 3 \times 34 = 102$ dof.

The NFRC of the blade's leading edge radial displacement r_1 is depicted in Fig. 11a. Same as in the previous sections, the employed numerical parameters, for which convergence has been reached, are $H = 80$ and $N = 2048$.

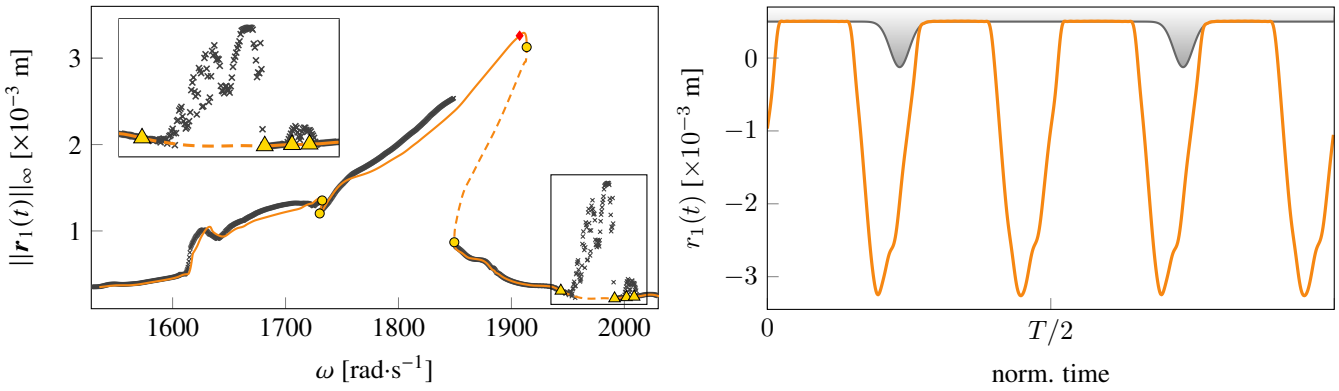

(a) Nonlinear frequency response curve, stable (—) and unstable (- - -) solutions, time integration (×)

(b) Time response at the nonlinear resonance (♦)

Figure 11 – Blade response with a deformed casing with centrifugal effects.

In agreement with the stiffening of the blade, the predicted nonlinear resonance occurs for $\omega \simeq 1900$ rad·s^{-1}, far above the value predicted in the previous section, see Fig. 9a. The corresponding time response, looking at the radial displacement of the blade's leading edge, is plotted in Fig. 11b. The superimposition of reference time integration results (×) still shows an excellent agreement with the RL-HBM. Same as for the configuration without centrifugal stiffening, it is evidenced that the solution obtained with time integration and null initial conditions always matches the lowest amplitude solution predicted by RL-HBM. Also, one may notice small, yet non-negligible discrepancies between amplitudes predicted in time and frequency domains for $\omega \in [1750,\ 1850]$ rad·s^{-1}. It is possible to confirm that these discrepancies are related to the distinct contact laws as it has been checked (but not shown here for brevity) that time integration with the same regularized contact law as the RL-HBM yields practically no error between the solutions.

Stability analysis carried out with Hill's method yields four limit points (●) and four Neimark-Sacker bifurcations (▲) that are consistent with the predicted NFRC and time integration results. Results obtained by both stability assessment methodologies are pictured in Fig. 12.

While similar trends are found, results are not perfectly identical due to the fact that a much higher number of harmonics and time steps would be required to converge with the Newmark $2n$-pass method. In agreement with observations made with the perfectly circular casing and the deformed casing without centrifugal stiffening, it is

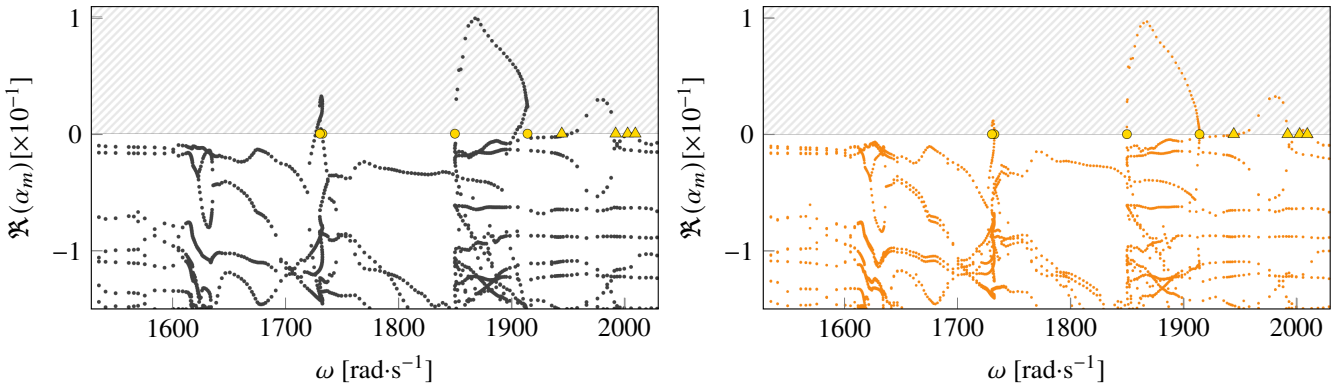

(a) Real part of Floquet exponents

(b) Real part of selected Hill's coefficients

Figure 12 – Application of the $2n$-pass method and Hill's method to the deformed casing contact configuration with centrifugal effects ($H = 80$, $N = 2048$).

evidenced here again that the convergence of the Newmark $2n$-pass method is significantly slower than the one of Hill's method, thus making it a less suitable option for the stability analysis of industrial blades undergoing unilateral contact constraints.

6 Conclusion

Building on the recent development of the RL-HBM, this paper deals with the stability analysis of an industrial compressor blade undergoing unilateral contact constraints. To the best of the author's knowledge, it is shown for the first time that, for such complex and severely nonlinear system, Hill's method converges significantly faster than the Newmark $2n$-pass method. Presented results on different contact configurations—featuring both a perfectly circular and a deformed casing, with and without centrifugal stiffening—all underline the relevance of bifurcation points obtained with Hill's method. These bifurcations match perfectly with phenomena observed with results obtained from a reference time domain solution method. Thus, they provide insight on physical phenomena that were observed but could not be explained before. While the asymptotical convergence of the Newmark $2n$-pass method towards results obtained with Hill's method is shown, it requires significantly higher values of both the number of retained harmonics and the number of time steps, thus yielding detrimental computational complexity. Nonetheless, despite of the fact that presented results demonstrate the applicability of Hill's method on industrial models, there remains theoretical challenges related to this approach. In particular, eigenvalue sorting remains sensitive as it was found that convergence of Hill's spectrum is dependent on the considered contact configuration.

Acknowledgments

This research was supported by the Canada Research Chairs Program (Funder ID: 10.13039/ 501100001804).

References

[1] Jacquet-Richardet, G., Torkhani, M., Cartraud, P., Thouverez, F., Baranger, T. N., Herran, M., Gibert, C., Baguet, S., Almeida, P. and Peletan, L. "Rotor to stator contacts in turbomachines. Review and application." *Mech. Syst. Sig. Process.* Vol. 40, No. 2 (2013): pp. 401–420. doi: 10.1016/j.ymssp.2013.05.010 - oai: hal-00934050.

[2] Krack, M., Salles, L. and Thouverez, F. "Vibration prediction of bladed disks coupled by friction joints." *Arch. Comput. Methods Eng.* Vol. 24, No. 3 (2017): pp. 589–636. doi: 10.1007/s11831-016-9183-2 - oai: hal-01825517.

[3] Siewert, C., Panning, L., Wallaschek, J. and Richter, C. "Multiharmonic Forced Response Analysis of a Turbine Blading Coupled by Nonlinear Contact Forces." *J. Eng. Gas Turbines Power* Vol. 132, No. 8. doi: 10.1115/1.4000266.

[4] Batailly, A., Legrand, M., Millecamps, A. and Garcin, F. "Numerical-experimental comparison in the simulation of rotor/stator interaction through blade-tip/abradable coating contact." *J. Eng. Gas Turbines Power* Vol. 134, No. 8 (2012): p. 11. doi: 10.1115/1.4006446 - oai: hal-00746632.

[5] Almeida, P., Gibert, C., Thouverez, F., Leblanc, X. and Ousty, J.-P. "Experimental analysis of dynamic interaction between a centrifugal compressor and its casing." *J. Turbomach.* Vol. 137, No. 3 (2015): p. 031008. doi: 10.1115/1.4028328 - oai: hal-01574149.

[6] Delhez, E., Nyssen, F., Golinval, J.-C. and Batailly, A. "Reduced order modeling of blades with geometric nonlinearities and contact interactions." *J. Sound Vib.* Vol. 500 (2021): p. 116037. doi: 10.1016/j.jsv.2021.116037 - oai: hal-03152678.

[7] Piollet, E., Nyssen, F. and Batailly, A. "Blade/casing rubbing interactions in aircraft engines: Numerical benchmark and design guidelines based on NASA rotor 37." *J. Sound Vib.* Vol. 460 (2019): p. 114878. doi: 10.1016/j.jsv.2019.114878 - oai: hal-02281666.

[8] Colaïtis, Y. and Batailly, A. "The harmonic balance method with arc-length continuation in blade-tip/casing contact problems." *J. Sound Vib.* Vol. 502 (2021): p. 116070. doi: 10.1016/j.jsv.2021.116070 - oai: hal-03163560.

[9] Colaïtis, Y. and Batailly, A. "Development of a Harmonic Balance Method-Based Numerical Strategy for Blade-Tip/Casing Interactions: Application to NASA Rotor 37." *J. Eng. Gas Turbines Power* Vol. 143, No. 11 (2021): p. 12. doi: 10.1115/1.4051967 - oai: hal-03286205.

[10] Bentvelsen, B. and Lazarus, A. "Modal and stability analysis of structures in periodic elastic states: application to the Ziegler column." *Nonlinear Dyn.* Vol. 91, No. 2 (2018): pp. 1349–1370. doi: 10.1007/s11071-017-3949-4 - oai: hal-01686514.

[11] Krack, M. and Gross, J. *Harmonic Balance for Nonlinear Vibration Problems.* Springer, Cham (2019). doi: 10.1007/978-3-030-14023-6.

[12] Petrov, E. P. "Stability Analysis of Multiharmonic Nonlinear Vibrations for Large Models of Gas Turbine Engine Structures With Friction and Gaps." *J. Eng. Gas Turbines Power* Vol. 139, No. 2 (2017): p. 022508. doi: 10.1115/1.4034353.

[13] Petrov, E. P. "A Method for Parametric Analysis of Stability Boundaries for Nonlinear Periodic Vibrations of Structures With Contact Interfaces." *J. Eng. Gas Turbines Power* Vol. 141, No. 3 (2018): p. 11. doi: 10.1115/1.4040850.

[14] Cardona, A., Lerusse, A. and Géradin, M. "Fast Fourier nonlinear vibration analysis." *Comput. Mech.* Vol. 22, No. 2 (1998): pp. 128–142. doi: 10.1007/s004660050347.

[15] Peletan, L., Baguet, S., Torkhani, M. and Jacquet-Richardet, G. "A comparison of stability computational methods for periodic solution of nonlinear problems with application to rotordynamics." *Nonlinear Dyn.* Vol. 72, No. 3 (2013): pp. 671–682. doi: 10.1007/s11071-012-0744-0 - oai: hal-00813265v1.

[16] Detroux, T., Renson, L., Masset, L. and Kerschen, G. "The harmonic balance method for bifurcation analysis of large-scale nonlinear mechanical systems." *Comput. Methods Appl. Mech. Eng.* Vol. 296 (2015): pp. 18–38. doi: 10.1016/j.cma.2015.07.017.

[17] Seydel, R. *Practical bifurcation and stability analysis.* Vol. 5. Springer, New York, NY (2009). doi: 10.1007/978-1-4419-1740-9.

[18] Von Groll, G. and Ewins, D. J. "The harmonic balance method with arc-length continuation in rotor/stator contact problems." *J. Sound Vib.* Vol. 241, No. 2 (2001): pp. 223–233. doi: 10.1006/jsvi.2000.3298 - oai: hal-01333704.

[19] Woiwode, L., Narayanaa Balaji, N., Kappauf, J., Tubita, F., Guillot, L., Vergez, C., Cochelin, B., Grolet, A. and Krack, M. "Comparison of two algorithms for Harmonic Balance and path continuation." *Mech. Syst. Sig. Process.* Vol. 136 (2020): p. 106503. doi: 10.1016/j.ymssp.2019.106503 - oai: hal-02424746.

[20] Cameron, T. M. and Griffin, J. H. "An alternating frequency/time domain method for calculating the steady-state response of nonlinear dynamic systems." *J. Appl. Mech.* Vol. 56, No. 1 (1989): pp. 149–154. doi: 10.1115/1.3176036 - oai: hal-01333697.

[21] Sarrouy, E. and Sinou, J.-J. "Non-Linear Periodic and Quasi-Periodic Vibrations in Mechanical Systems - On the use of the Harmonic Balance Methods." Ebrahimi, F. (ed.) *Advances in Vibration Analysis Research*, Chap. 21. IntechOpen, Rijeka (2011): pp. 419–434. doi: 10.5772/15638 - oai: hal-00730895.

[22] Guckenheimer, J. and Holmes, P. "Local Bifurcations." *Nonlinear oscillations, dynamical systems, and bifurcations of vector fields*. Springer, New York (1983): pp. 117–165. doi: 10.1007/978-1-4612-1140-2_3.

[23] Moore, G. "Floquet theory as a computational tool." *SIAM J. Numer. Anal.* Vol. 42, No. 6 (2005): pp. 2522–2568. doi: 10.1137/S0036142903434175.

[24] Zhou, J., Hagiwara, T. and Araki, M. "Spectral characteristics and eigenvalues computation of the harmonic state operators in continuous-time periodic systems." *Systems & Control Letters* Vol. 53, No. 2 (2004): pp. 141 – 155. doi: 10.1016/j.sysconle.2004.03.002.

[25] Thomas, O., Lazarus, A. and Touzé, C. "A harmonic-based method for computing the stability of periodic oscillations of non-linear structural systems." *Proceedings of the ASME IDETC/CIE 2010*: pp. 883–892. 2010. doi: 10.1115/DETC2010-28407 - oai: hal-01148758.

[26] Huebler, D. "Rotor 37 and stator 37 assembly. Records of the National Aeronautics and Space Administration, 1903 - 2006. Photographs relating to agency activities, facilities and personnel, 1973 - 2013." https://catalog.archives.gov/id/17468361, 1977 (accessed 2020-10-29).

[27] Reid, L. and Moore, R. D. "Design and overall performance of four highly loaded, high speed inlet stages for an advanced high-pressure-ratio core compressor." Technical report no., NASA Lewis Research Center Cleveland, OH, United States. Url : `https://ntrs.nasa.gov/citations/19780025165`, 1978 (accessed 2020-10-29).

[28] Craig Jr, R. R. and Bampton, M. C. C. "Coupling of substructures for dynamic analyses." *AIAA J.* Vol. 6, No. 7 (1968): pp. 1313–1319. doi: 10.2514/3.4741.

[29] Sternchüss, A. and Balmès, E. "On the reduction of quasi-cyclic disk models with variable rotation speeds." *Proceedings of the Int. Conference on Adv. Acoustics and Vib. Eng.*: pp. 3925–3939. 2006. oai: hal-00266394.